

# Non-avalanche single photon detection without carrier transit-time delay through quantum capacitive coupling

YANG ZHANG,<sup>1,4</sup> YANG WU,<sup>2</sup> XIAOXIN WANG,<sup>3</sup> ERIC R. FOSSUM,<sup>3</sup> RAHUL KUMAR,<sup>2</sup> JIFENG LIU,<sup>3,5</sup> GREGORY SALAMO,<sup>2</sup> AND SHUI-QING YU<sup>1,6</sup>

<sup>1</sup>Department of Electrical Engineering, University of Arkansas, Fayetteville, AR 72701, USA

<sup>2</sup>Department of Physics, University of Arkansas, Fayetteville, AR 72701, USA

<sup>3</sup>Thayer School of Engineering, Dartmouth College, Hanover, NH 03755, USA

<sup>4</sup>yangzh08@gmail.com

<sup>5</sup>Jifeng.Liu@dartmouth.edu

<sup>6</sup>syu@uark.edu

**Abstract:** Searching for innovative approaches to detect single photons remains at the center of science and technology for decades. This paper proposes a zero transit-time, non-avalanche quantum capacitive photodetector to register single photons. In this detector, the absorption of a single photon changes the wave function of a single electron trapped in a quantum dot (QD), leading to a charge density redistribution nearby. This redistribution translates into a voltage signal through capacitive coupling between the QD and the measurement probe. Using InAs QD/AlAs barrier as a model system, the simulation shows that the output signal reaches ~4 mV per absorbed photon, promising for high-sensitivity, ps single-photon detection.

© 2017 Optical Society of America

**OCIS codes:** (040.5160) Photodetectors; (230.5160) Photodetectors; (230.0230) Optical devices.

## References and links

1. U. Hilleringmann and K. Goser, "Optoelectronic system integration on silicon: waveguides, photodetectors, and VLSI CMOS circuits on one chip," *IEEE Trans. Electron Dev.* **42**, 841–846 (1995).
2. H. Izuo, "Optoelectronic Devices and Material Technologies for Photo-Electronic Integrated Systems," *Jpn. J. Appl. Phys.* **32**, 266 (1993).
3. F. H. L. Koppens, T. Mueller, P. Avouris, A. C. Ferrari, M. S. Vitiello, and M. Polini, "Photodetectors based on graphene, other two-dimensional materials and hybrid systems," *Nat. Nanotechnol.* **9**(10), 780–793 (2014).
4. S. R. Forrest, "Optoelectronic integrated circuits," *Proc. IEEE* **75**, 1488–1497 (1987).
5. B. E. Jones, "Optical fibre sensors and systems for industry," *J. Phys. Educ.* **18**(9), 770 (1985).
6. L. Becker, "Influence of IR sensor technology on the military and civil defense," *Proc. SPIE* **6127**, 61270S (2006).
7. T. Oto, R. G. Banal, K. Kataoka, M. Funato, and Y. Kawakami, "100 mW deep-ultraviolet emission from aluminium-nitride-based quantum wells pumped by an electron beam," *Nat. Photonics* **4**, 767–770 (2010).
8. E. R. Fossum, "CMOS image sensors: electronic camera-on-a-chip," *IEEE Trans. Electron Dev.* **44**, 1689–1698 (1997).
9. E. R. Fossum and D. B. Hondongwa, "A Review of the Pinned Photodiode for CCD and CMOS Image Sensors," *IEEE J. Electron. Dev. Soc.* **2**, 33–43 (2014).
10. R. H. Hadfield, "Single-photon detectors for optical quantum information applications," *Nat. Photonics* **3**, 696–705 (2009).
11. Y. Zhang, Y. Yuan, and J. Huang, "Detecting 100 fW cm<sup>-2</sup> Light with Trapped Electron Gated Organic Phototransistors," *Adv. Mater.* **29**(5), 1603969 (2017).
12. U. Akgun, A. S. Ayan, G. Aydin, F. Duru, J. Olson, and Y. Onel, "Afterpulse timing and rate investigation of three different Hamamatsu Photomultiplier Tubes," *J. Instrum.* **3**, T01001 (2008).
13. H. Photonics, *Photomultiplier tubes, basics and applications* (Hamamatsu, 2006).
14. M. D. Eisaman, J. Fan, A. Migdall, and S. V. Polyakov, "Single-photon sources and detectors," *Rev. Sci. Instrum.* **82**(7), 071101 (2011).
15. M. Teich, K. Matsuo, and B. Saleh, "Excess noise factors for conventional and superlattice avalanche photodiodes and photomultiplier tubes," *IEEE J. Quantum Electron.* **22**, 1184–1193 (1986).
16. S. Cova, M. Ghioni, A. Lacaita, C. Samori, and F. Zappa, "Avalanche photodiodes and quenching circuits for single-photon detection," *Appl. Opt.* **35**(12), 1956–1976 (1996).

17. J. C. Blakesley, P. See, A. J. Shields, B. E. Kardynal, P. Atkinson, I. Farrer, and D. A. Ritchie, "Efficient Single Photon Detection by Quantum Dot Resonant Tunneling Diodes," *Phys. Rev. Lett.* **94**(6), 067401 (2005).
18. F. Marsili, V. B. Verma, J. A. Stern, S. Harrington, A. E. Lita, T. Gerrits, I. Vayshenker, B. Baek, M. D. Shaw, R. P. Mirin, and S. W. Nam, "Detecting single infrared photons with 93% system efficiency," *Nat. Photonics* **7**, 210–214 (2013).
19. J. S. Andrew, P. O. S. Martin, F. Ian, A. R. David, L. L. Mark, K. P. Nalin, A. H. Richard, E. N. Carl, J. C. Neil, and P. Michael, "Single Photon Detection with a Quantum Dot Transistor," *Jpn. J. Appl. Phys.* **40**, 2058 (2001).
20. W. Du, H. Inokawa, H. Satoh, and A. Ono, "SOI metal-oxide-semiconductor field-effect transistor photon detector based on single-hole counting," *Opt. Lett.* **36**(15), 2800–2802 (2011).
21. E. J. Gansen, M. A. Rowe, M. B. Greene, D. Rosenberg, T. E. Harvey, M. Y. Su, R. H. Hadfield, S. W. Nam, and R. P. Mirin, "Photon-number-discriminating detection using a quantum-dot, optically gated, field-effect transistor," *Nat. Photonics* **1**, 585–588 (2007).
22. J. Ma and E. R. Fossum, "Quanta image sensor jot with sub 0.3 e-rms read noise and photon counting capability," *IEEE Electron Device Lett.* **36**(9), 926–928 (2015).
23. E. R. Fossum, J. Ma, S. Masoodian, L. Anzagira, and R. Zizza, "The quanta image sensor: Every photon counts," *Sensors (Basel)* **16**(8), 1260 (2016).
24. S. M. Sze and K. K. Ng, *Physics of Semiconductor Devices, 3rd Ed* (Wiley-Interscience, 2006).
25. J. E. Bowers and Y. G. Wey, "High Speed Photodetectors", in *Handbook of Optics, Vol. 1, 2nd Ed*, M. Bass, ed. (McGraw-Hill New York, 1995), Chap. 17.
26. DARPA solicitation DARPA-BAA-16-25, "Fundamental Limits of Photon Detection," <https://www.fbo.gov/index?s=opportunity&mode=form&id=6d13cf57d50d88aef23e77a0ca3d4ba&tab=core&cvview=0>.
27. S. Funk, G. Acuna, M. Handloser, and R. Kersting, "Probing the momentum relaxation time of charge carriers in ultrathin layers with terahertz radiation," *Opt. Express* **17**(20), 17450–17456 (2009).
28. P. Borri, W. Langbein, S. Schneider, U. Woggon, R. L. Sellin, D. Ouyang, and D. Bimberg, "Ultralong dephasing time in InGaAs quantum dots," *Phys. Rev. Lett.* **87**(15), 157401 (2001).
29. K. K. Likharev, "Single-electron devices and their applications," *Proc. IEEE* **87**(4), 606–632 (1999).
30. Z. M. Wang, K. Holmes, J. L. Shultz, and G. J. Salamo, "Self-assembly of GaAs holed nanostructures by droplet epitaxy," *Phys. Status Solidi., A Appl. Mater. Sci.* **202**, R85–R87 (2005).
31. H. Grabert and M. H. Devoret, *Single charge tunneling: Coulomb blockade phenomena in nanostructures*, (Plenum Press, 1992).
32. M. Sugawara, K. Mukai, and H. Shoji, "Effect of phonon bottleneck on quantum-dot laser performance," *Appl. Phys. Lett.* **71**, 2791–2793 (1997).
33. J. Liu, M. Zhou, L. Ying, X. Chen, and Z. Yu, "Enhancing the optical cross section of quantum antenna," *Phys. Rev. A* **95**(1), 013814 (2017).
34. M. Levinshstein, S. Rumyantsev, and M. Shur, *Handbook Series on Semiconductor Parameters* (Word Scientific Publishing, 1996).
35. R. V. N. Melnik and M. Willatzen, "Bandstructures of conical quantum dots with wetting layers," *Nanotechnology* **15**, 1 (2004).
36. I. Vurgaftman, J. R. Meyer, and L. R. Ram-Mohan, "Band parameters for III–V compound semiconductors and their alloys," *J. Appl. Phys.* **89**, 5815–5875 (2001).
37. Z. Z. Lwin, K. L. Pey, N. Raghavan, Y. Chen, and S. Mahapatra, "New Leakage Mechanism and Dielectric Breakdown Layer Detection in Metal-Nanocrystal-Embedded Dual-Layer Memory Gate Stack," *IEEE Electron Device Lett.* **32**, 800–802 (2011).
38. J. H. Lee, Z. M. Wang, N. W. Strom, Y. I. Mazur, and G. J. Salamo, "InGaAs quantum dot molecules around self-assembled GaAs nanomound templates," *Appl. Phys. Lett.* **89**, 202101 (2006).
39. Q. Li, Y. Wan, A. Y. Liu, A. C. Gossard, J. E. Bowers, E. L. Hu, and K. M. Lau, "1.3- $\mu\text{m}$  InAs quantum-dot micro-disk lasers on V-groove patterned and unpatterned (001) silicon," *Opt. Express* **24**(18), 21038–21045 (2016).
40. ITRS. Reports, "2015 ITRS 2.0," <http://www.itrs2.net/itrs-reports.html>.
41. K. H. Goh, S. Yadav, K. L. Low, G. Liang, X. Gong, and Y. C. Yeo, "Gate-All-Around In<sub>0.53</sub>Ga<sub>0.47</sub>As Junctionless Nanowire FET With Tapered Source/Drain Structure," *IEEE Trans. Electron Dev.* **63**(3), 1027–1033 (2016).
42. V. Grigel, D. Dupont, K. De Nolf, Z. Hens, and M. D. Tessier, "InAs colloidal quantum dots synthesis via aminonictogen precursor chemistry," *J. Am. Chem. Soc.* **138**(41), 13485–13488 (2016).
43. V. R. Manfrinato, D. D. Wanger, D. B. Strasfeld, H. S. Han, F. Marsili, J. P. Arrieta, T. S. Mentzel, M. G. Bawendi, and K. K. Berggren, "Controlled placement of colloidal quantum dots in sub-15 nm clusters," *Nanotechnology* **24**(12), 125302 (2013).
44. E. J. Gansen, M. A. Rowe, D. Rosenberg, M. Greene, T. E. Harvey, M. Y. Su, R. H. Hadfield, S. W. Nam, and R. P. Mirin, "Single-photon detection using a semiconductor quantum dot, optically gated, field-effect transistor," in *Lasers and Electro-Optics, 2006 and 2006 Quantum Electronics and Laser Science Conference* (IEEE, 2006), pp. 1–2.
45. J. Kim and J. F. Buckwalter, "Staggered gain for 100+ GHz broadband amplifiers," *IEEE J. Solid-State Circuits* **46**(5), 1123–1136 (2011).

46. S. P. Voinigescu, S. Shopov, J. Bateman, H. Farooq, J. Hoffman, and K. Vasilakopoulos, "Silicon Millimeter-Wave, Terahertz, and High-Speed Fiber-Optic Device and Benchmark Circuit Scaling Through the 2030 ITRS Horizon," *Proc. IEEE* **105**(6), 1087–1104 (2017).
47. B. I. Abdulrazzaq, O. J. Ibrahim, S. Kawahito, R. M. Sidek, S. Shafie, N. A. M. Yunus, L. Lee, and I. A. Halin, "Design of a Sub-Picosecond Jitter with Adjustable-Range CMOS Delay-Locked Loop for High-Speed and Low-Power Applications," *Sensors (Basel)* **16**(10), 1593 (2016).
48. C. H. Fields, T. Tsen, C. McGuire, Y. Yoon, D. Zehnder, S. Thomas, M. Montes, I. Valles, J. Duvall, and T. Hussain, "110+ GHz Transimpedance Amplifier in InP-HBT Technology for 100 Gbit Ethernet," *IEEE Microw. Wirel. Compon. Lett.* **20**(8), 465–467 (2010).
- 49Q.-Y. Zhao, D. Zhu, N. Calandri, A. E. Dane, A. N. McCaughan, F. Bellei, H.-Z. Wang, D. F. Santavicca, and K. K. Berggren, "Single-photon imager based on a superconducting nanowire delay line," *Nat. Photonics* **11**, 247–251 (2017).

## 1. Introduction

Photodetectors are indispensable components in most optoelectronic systems [1–4]. They are widely used in industry [5], military [6], scientific research [7], and more recently in consumer electronics applications [8,9]. In terms of functionality, photodetectors are essentially converters that absorb light and pass the information carried by the light to an electrical output (a current or voltage signal). Among all the types, photodetectors capable of registering single photons, namely single-photon detectors (SPDs), are recently attracting tremendous interest. They are highly desirable for optical quantum information applications which are now at the forefront of science and technology [10]. In general, the detection of extremely weak optical signals (e.g., a single photon) requires the presence of an amplification mechanism in the detector that gives rise to a detectable electrical signal as an output [11]. In single-photon detectors, this amplification is often enabled by a large internal gain which is defined as the number of charges generated per absorbed photon. For example, photomultiplier tubes (PMTs) can readily reach an internal gain of  $\sim 10^6$ - $10^8$  through a cascade electron multiplication process in vacuum tubes [12,13], and single-photon avalanche photodiodes (SPADs) can amplify a single photon signal by a photon-triggered avalanche process occurring in semiconductors [14]. Despite their popularity in single-photon detection, PMTs and SPADs have apparent disadvantages. For instance, PMTs require high voltage ( $\sim 1000$  V) to operate [13], while SPADs' avalanche process comes inherently with large internal noise [15]. In addition, SPADs require a quenching mechanism to cease the charge multiplication [16].

Driven by increasingly strict requirements for quantum information applications, the search for new single-photon detectors has been a topic under intensive investigation over the past decades [10,14]. In 2005, Blakesley and associates demonstrated efficient single-photon detection using quantum dot resonant tunneling diodes, where the single-photon generated hole was captured in quantum dots (QDs) grown close to the double barriers and thus affected the resonant tunnel current through the diode [17]. Highly efficient superconducting nanowire single-photon detectors which utilized the normal-superconducting transition induced by local photon energy deposition have been developed by Marsili and associates [18], yet it inevitably requires cryogenic temperatures. In addition, detection schemes utilizing the modulation of the channel conductance by single-photon generated charges have been demonstrated on detectors constructed from field effect transistors [19–21]. Most recently, Si quanta image sensors (QIS) achieved room-temperature, non-avalanche single photon detection by transferring the photoelectron to an ultralow capacitance ( $C \sim 400$  aF) floating diffusion region such that a photovoltage conversion gain of  $\Delta V = e/C \sim 0.4$  mV was achieved per photoelectron [22,23]. This conversion gain is well above the noise level of  $\sim 0.1$  mV in 65 nm complementary metal-oxide-semiconductor technology (CMOS) node and enables high-sensitivity single photon detection.

Despite of all these efforts, so far most semiconductor single photon detectors still rely on the transport of photogenerated carriers, leading to carrier transit-time limited bandwidth [24] and timing jitter. While RC limited bandwidth has been addressed by traveling wave

photodetectors [25], the transit-time has limited the response time to several ps, or sub-THz bandwidth. For many applications, such as high-performance light detection and ranging (LIDAR) systems based on time-of-flight photon detection, it is highly desirable to further reduce the response time and timing jitter below 1 ps in order to improve the time resolution [26]. Deep sub-ps photodetection can also help to retrieve more information from the incident photons before electron-phonon scattering and thermalization, which typically happens in 0.2-1 ps scale at room temperature [27,28]. Now the question is: can we achieve single photon detection without carrier transport process at all? If so, we have an approach to break through the transit-time limit.

In this article, we propose a fundamentally new scheme to detect single photons. In this scheme, the change in the wave function of a quantum-confined carrier upon absorption of a single photon leads to a charge density redistribution around the QD. The charge density redistribution translates to an appreciable voltage output signal on a nearby probe through quantum capacitive coupling. Similar to the scenario in single electron transistors (SETs) [29], the output voltage is proportional to  $1/C$ , where  $C$  is a small effective capacitance ( $\sim 1$ -100 aF) between the QD and the probe. We term this detector a quantum capacitive photodetector (QCP) because the charge density redistribution due to the change in the wave function upon optical excitation is a quantum mechanical phenomenon rather than a classical one. In contrast to other photodetectors reported to date, QCP does not rely on carrier transport or multiplication process to generate the output signal. Thus, the response time, timing jitter and noise, which are important figures of merit of photodetectors, may be minimized. Furthermore, the elimination of the carrier transport minimizes the power consumption of photon detection. Conventionally, photodetectors operating in photovoltaic mode tends to be slow due to the finite drift velocity, yet QCPs circumvent this issue by substituting the carrier transport with quantum capacitive coupling. To illustrate the concept of QCP, we consider a model system where a single electron is trapped in an InAs QD embedded in AlAs (e.g. through single electron tunneling and Coulomb blockade in an SET-like structure), and we solve Schrödinger's and Poisson's equations in COMSOL to evaluate the amplitude of the output voltage signal. For an ideal point probe positioned 5 nm away from the tip of a cone-shaped InAs QD, we obtain a maximum potential change of  $\sim 4$  mV for QD radius of 9 nm, which is a voltage signal that can be readily picked up by modern nanoelectronic circuitry. Our results show that the proposed QCP that harnesses the quantum nature of electrons may open a new avenue for single-photon detections.

## 2. Description of the model and simulation procedure

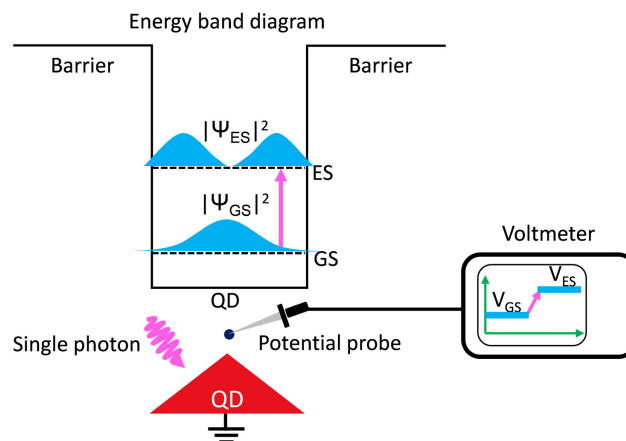


Fig. 1. Variation of the electron distribution probability around a QD (in red) upon single-photon absorption. GS and ES denote the electron ground and first excited states, respectively.  $|\Psi|^2$  is the electron distribution probability, and its profile is sketched in blue.

For an electron confined in a QD, the shape of its wave function, and therefore the electron distribution probability, varies when the electron is situated in different states, as illustrated in Fig. 1. When the electron is excited from the ground state to an excited state by a single photon, this change in the wave function and electron density distribution gives rise to a voltage output signal at a probing location near the QD through capacitive coupling according to Poisson's equation. This is the basic idea that constitutes the working mechanism of the proposed QCP. It probes directly the change in the electron's wave function upon optical excitation without relying on any charge transport process, thereby breaking through the transit-time limit. Since there is no charge transporting through the device, QCPs minimize the energy consumption and maximize the speed of photodetection simultaneously. In the following, we outline the simulation procedure.

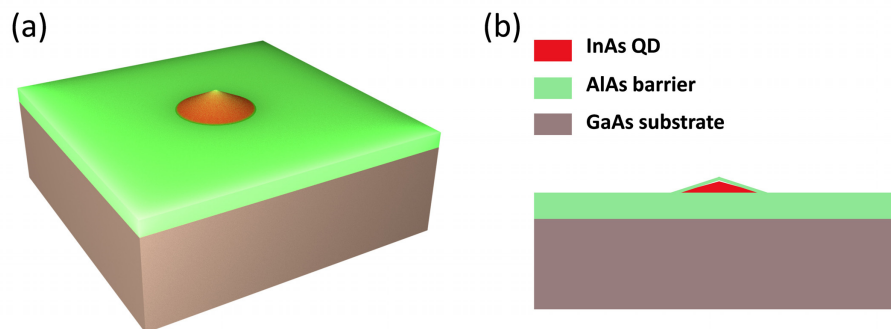


Fig. 2. Schematic diagram of the model system used for simulation: 3-dimensional (a) and cross-sectional (b) views.

Figure 2 illustrates the model system used for our simulation. Here a single cone-shaped InAs QD is buried in an AlAs barrier layer grown on a GaAs substrate. The wetting layer is omitted in Fig. 2, as we assume that the QD is grown by the “droplet epitaxy” method [30]. As an initial condition, we assume that the InAs QD is populated with a single electron situated in the ground state, as shown in Figs. 3(a) and 3(b). This can be implemented via electron tunneling and Coulomb blockade in a device structure similar to SETs [32]. When a single photon with an energy of  $\Delta E$  is absorbed by the QD, the electron is promoted from the ground state (GS) to the first excited state (ES). Hereafter, we use ES to denote the first excited state, unless otherwise stated. Here  $\Delta E$  is the energy spacing between these two states. We solve the single-electron effective-mass Schrodinger's equation in a finite potential well (Figs. 3(a) and 3(b)) and obtain the GS and ES wave functions. Using the probabilistic interpretation of wave function, GS and ES wave functions can be translated into charge distributions around the QD given a certain duration of time, through the relationship  $\rho = e|\Psi|^2$ , where  $\rho$  is the charge density in space,  $e$  is the elementary charge, and  $\Psi$  is the single-electron wave function. These charge densities are then fed into the Poisson's equation to find the potential distributions around the QD for the GS and the ES cases. The difference between these two potential distributions at specified locations near the QD is considered the output voltage signal associated with a single photon absorption event. After a lifetime  $\tau_{es}$  the electron relaxes back to the GS by emitting phonons to the surroundings, the detector is then back to its initial condition and ready for detecting the next photon. We note that the detector proposed here responds to one photon at a time since there is only one electron sitting in the ground state. The measurement of the output voltage signal should be performed within  $\tau_{es}$ , which typically ranges from fs to ps, and can be prolonged to ns, if the so-called phonon bottleneck effect is invoked by carefully controlling the QD size such that the energy spacing between the ES and the GS is not an integer times the phonon energy [33]. Therefore, the lifetime  $\tau_{es}$  is essentially the time needed to reset the QCP and can be engineered for targeted applications.

Using the computed wave functions from the Schrödinger's equation, we have also evaluated the transition matrix elements between the GS and the ES. While a single photon polarized either in-plane or out-of-plane can induce electron excitation in all cases, the matrix element of the former is usually 3 to 10 times larger than that of the latter. Correspondingly, the intraband absorption coefficient for in-plane polarized photon is 2000-6000  $\text{cm}^{-1}$ , on the same order of that of the interband absorption. This result indicates that the InAs QDs are better suited for surface normal photon detection. While a single QD has limited optical absorption, it can be greatly enhanced by photon management [34] and/or vertically stacked QD arrays with individual output voltage readout from each QCP. In the latter case, we can also resolve the exact location of the photon absorption event, which is highly relevant to quantum information.

### 3. Results and discussion

#### 3.1 Single-electron wave function and charge distribution

The single-electron GS and ES wave functions were found by following the work of R. V. N. Melnik and M. Willatzen [35]. Geometric and material parameters for the simulation in COMSOL are summarized in Tab. 1 and Tab. 2, respectively. The results shown in Fig. 3 and Fig. 4 were obtained with QD of 10 nm radius and 5 nm height. The conduction band offset was taken as 1.94 eV, as indicated in Figs. 3(a) and 3(b) [36]. The variation of the band offset due to strain is neglected in this simulation for simplicity. The energy spacing between the ES and the GS is 225.8 meV for a QD radius of  $r = 10$  nm, which can be adjusted by controlling the QD radius or height, and the corresponding quantum confinement effect. The cross-sections of the calculated charge density in the QD are exhibited in Figs. 3(e) and 3(f) for GS and ES, respectively. These charge densities have been divided by the elementary charge to give a fraction value. It is obvious that the single electron charge is well confined in the QD in Fig. 3. The charge distribution is more localized towards the center of the QD for the GS, while it is spread towards the edge of the QD for the ES. We remark that this difference in the shape of the charge distribution directly gives rise to the potential difference (output voltage signal) at a specified location near the QD. This can be understood heuristically as follows. The electric potential  $V$  due to an electron can be expressed as

$$V = \frac{-e}{4\pi\epsilon_0\epsilon_r r} \quad (1)$$

where  $\epsilon_0$  is the vacuum permittivity, and  $\epsilon_r$  is the relative permittivity,  $e$  is the elementary charge, and  $r$  is the distance between the electron and the location for potential measurement. Difference in the shape of charge distribution shown in Figs. 3(e) and 3(f). leads to a difference in the average distance  $r$  (in Eq. (1)) between the charge and a properly selected probe location, and eventually results in a change in the electric potential. For example, a top probe on the positive  $z$ -axis obviously has a larger distance  $r_2$  to the (negative) charge distribution in Fig. 3(f) (excited state) than  $r_1$  in Fig. 3(e) (ground state), thereby sensing a positive change in the potential upon excitation. The denominator in Eq. (1) ( $4\pi\epsilon_0\epsilon_r r$ ) can be viewed as the self-capacitance of a sphere with a radius of  $r$  [37]. This is the reason why we name this type of device quantum capacitive photodetector.

**Table 1. Geometric parameters used in simulation**

Name	Value
Quantum dot height	2-15 nm
Quantum dot radius	4-30 nm
Top barrier thickness	2 nm

Table 2. Material parameters used in simulation [31]

Material	Relative permittivity	Electron effective mass ( $m_0$ )	Hole effective mass ( $m_0$ )	Electron affinity (eV)
InAs	15.15	0.023	0.41	4.9
AlAs	10.06	0.2623	0.76	3.5
GaAs	12.9	0.063	0.51	-

$m_0$  is the electron rest mass.

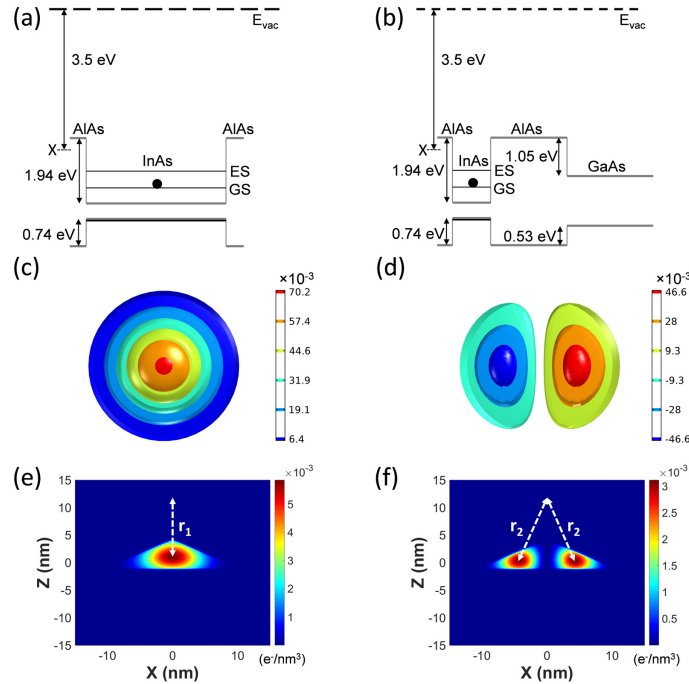


Fig. 3. Energy band diagram of the InAs/AlAs model system in equilibrium along an axis parallel (a) or perpendicular (b) to the substrate. The black dot represents a single electron sitting in the ground state.  $X$  denotes the  $X$  point of the conduction band of AlAs from which the electron affinity is measured [31]. (c) and (d) are top views of normalized GS and ES (real part) wave functions of a single electron trapped in the QD, respectively. (e) and (f) are color-coded mapping of normalized charge distribution on the  $x$ - $z$  plane across the center of the QD for the GS and ES, respectively.  $r_1$  ( $r_2$ ) is the effective distance between the top probe and the GS (ES) charge distribution, as described in the main text.

### 3.2 Potential difference (output signal) around the QD

The electric potential around the QD due to a single electron was calculated using the Poisson's equation, and the results are presented in Figs. 4(a) and 4(b) for the GS and the ES cases, respectively. To obtain the potential difference in space, the potential distribution for the GS case (Fig. 4(a)) was subtracted directly from the potential distribution for the ES case (Fig. 4(b)) and the difference is displayed in Fig. 4(c). Remarkably, finite potential differences of the order of mV were found near the QD, which were considered the output signal of the single-photon detector proposed here.

In practical measurements, it is desired that the output signal from the single-photon detector is as large as possible. To study the variation of the output signal under different circumstances, we positioned two imaginary potential probes near the QD: one was above the QD (top probe) and the other was to the side of the QD (side probe), as shown in the inset of Fig. 4(d). We first investigated the dependence of the output signal on the distance between

the probe location and the QD. The distances for top and side probes were measured from the tip and edge of the QD, respectively. As expected, the output signal vanished while moving the probes away from the QD, and increased while the probes approached the QD (Fig. 4(d)). For example, when the probes were 4.8 nm away from the QD, output signals on top and side probes were 4 mV and  $-0.16$  mV, respectively. The top probe signal was more than one order of magnitude larger than the side probe signal, suggesting that the top probe position was a more favorable location for taking potential measurement than the side probe position. Meanwhile, the top probe signal was also much higher than the signal of QIS ( $\sim 0.4$  mV per photoelectron), which can be readily picked up by sophisticated instruments given that the voltage measurement is done within the electron ES lifetime  $\tau_{es}$ . Further reducing the probe-QD distance from 5 nm may lead to even larger output signals (Fig. 4(d)). We note, however, that this distance reduction may also increase the chance of electron tunneling from the QD to probes and thus disturb the measurement. Therefore, optimal probe distances ought to be determined when reading out output signals in experiments.

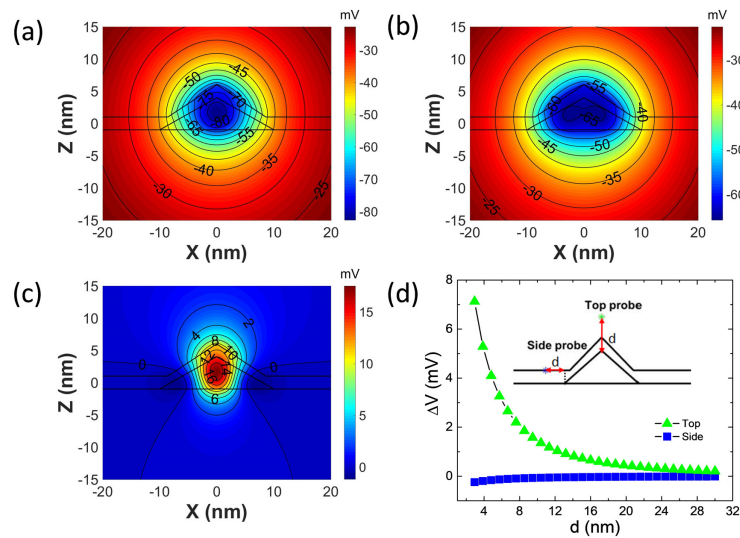


Fig. 4. Potential distribution in space induced by a single electron in the ground state (a) and in the excited state (b). (c) displays the potential difference ( $\Delta V = V_{es} - V_{gs}$ ) in space. The contour lines in (a)-(c) are labeled with potential values. (d) Potential difference (output signal) at top (green) and side (blue) probe locations as marked in the inset while changing the distance  $d$  between the probes and the InAs QD.

### 3.3 Effect of QD size and shape on output signal

For QDs grown by the molecular beam epitaxy (MBE) system, there naturally exists a variation in the QD size. Therefore, we examined the dependence of the output signal on the QD size. To keep the shape of the QD unchanged, the ratio of the QD radius over its height was fixed to 2 while changing the radius from 4 nm to 30 nm. Unless otherwise stated, the side probe was positioned 5 nm away from the edge of the QD, and the top probe was positioned on the symmetric axis of the QD geometry and 5 nm above the highest point of the QD. Interestingly, there existed an optimal QD radius to generate a maximum output signal for each probe locations (Fig. 5). For example, the output measured with top probe peaked at  $\sim 3.9$  mV when the QD radius was 9 nm. Output signals decreased as the QD radius departed from respective optimal values. This can be rationalized by using the heuristic model described in Sec. 3.1. For smaller QDs that still confines  $>50\%$  of the excited state wave function within the InAs regions, the charges are generally less spread in the radial directions upon excitation (in reference to Fig. 3(f)) and thus the output signal decreases. Note that this



scenario could change if the confinement of the wave function within the QD greatly decreases upon excitation, as will be discussed in a separate work. As the QD radius increases, the charge density is spread more in the radial directions upon excitation to give a bigger change in the effective distance from the probe, and the output signal rises and reaches a maximum. Further increase of the radius, however, starts to diminish the quantum effect and the differences between the wave functions of the ground and excited states. The latter weighs the output signal down as QD radius further increases.

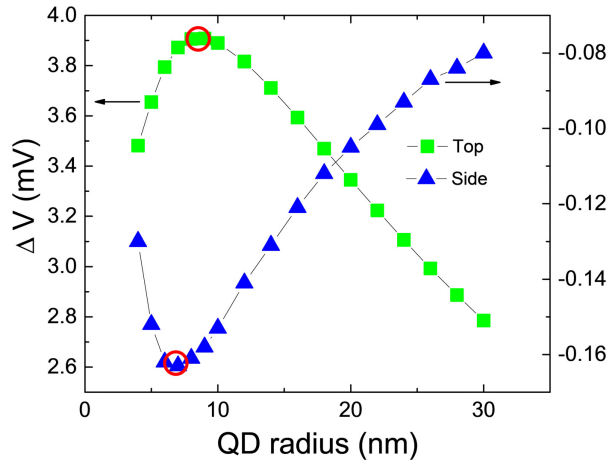


Fig. 5. Effect of QD shape on the detector output signal at top and side probe locations. All QDs have a bottom radius of 10 nm and a height of 5 nm. The profiles of the QDs are sketched above the corresponding histograms.

The shape of the QD may also influence the output signal by changing the symmetry or shape of the charge distribution in the QD. Figure 6 shows histograms of the output signal at top and side probe locations derived from QDs of three shapes, namely, volcano, disk and cone shapes. All these shapes can be achieved in realistic growth [38,39]. We found that the cone-shaped QD offered the largest output signal at the top probe location among the three while the disk-shaped QD excelled with output signal measured at the side probe location. This result suggests that QD shape engineering together with proper positioning of the probe can help achieve optimal detector output signal.

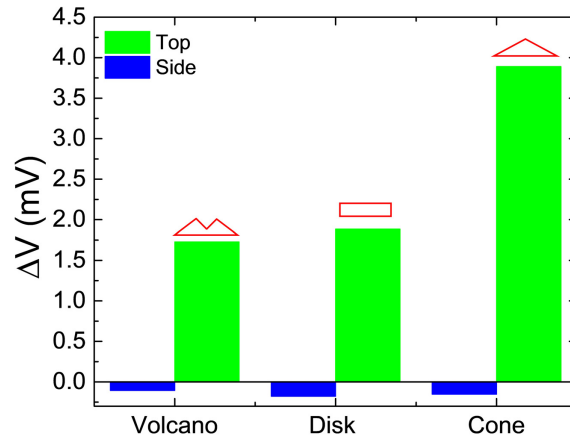


Fig. 6. Output signal detected at top (green) and side (blue) probe locations while changing the radius of the QD. Red circles indicate the maximum outputs. All QDs have a bottom radius of 10 nm and a height of 5 nm.

### 3.4 An example of readout scheme

To read out the potential signals in Fig. 4(d) and Fig. 5, the QD needs to interface with an external circuitry. Since the electron relaxation from the ES to the GS is a relatively fast process (with a timescale of fs to ns, see the discussion in Sec. 2), a high-speed readout circuitry is of paramount importance to catch the signal. Below we describe a possible scheme (Fig. 7) that may fulfil the requirements for low-noise and high-speed readouts. In this scheme, the QD is placed atop the gate of a field effect transistor (FET) with a reasonably high transconductance, e.g. several mS from state-of-the-art sub-14 nm CMOS technology [40]. Note that the ultralow capacitance of  $\sim 10$  aF for sub-14 nm MOSFETs is much smaller than that of the QCP itself ( $e/\Delta V \sim 40$  aF for  $\Delta V \sim 4$  mV), thereby allowing efficient transfer of the single photon induced  $\Delta V$  to the gate. The FETs can also adopt an InGaAs nanowire all-around structure that can be readily integrated with the GaAs substrate [41]. InAs colloidal QDs can be synthesized by a wet chemical method [42]. Between the QD and the gate is a thin ( $\sim 5$  nm) insulating layer, which can be precisely controlled by modern fabrication technology such as atomic layer deposition. The precise placement of the QD can be realized, for example, by a lift-off process demonstrated in Ref [43]. Similar to the situation in Ref [44], the single-photon induced potential change  $\Delta V$  is translated into a current change  $\Delta I$  by a FET through a transconductance  $g_m$  (Fig. 7). For example, with a  $g_m = 3$  mS and a  $\Delta V = 4$  meV per absorbed photon, we have  $\Delta I = 12$   $\mu$ A induced by a single photon. Then the  $\Delta I$  is amplified and converted to a voltage output  $V_O$  by a high-speed transimpedance amplifier (TIA).

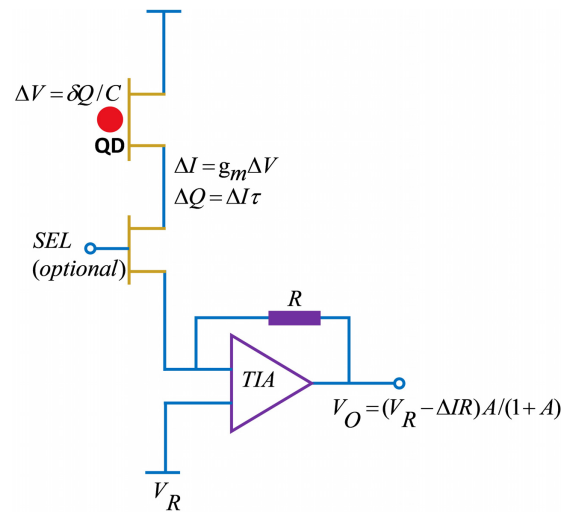


Fig. 7. A possible readout scheme for QCP. SEL stands for an optional FET that can be used to enable/disable the measurement. The equation provides the relationship between the FET channel current change and the TIA output voltage.  $\delta Q$  is an equivalent charge change on the QD,  $C$  is the coupling capacitance between the QD and the gate,  $\Delta Q$  is the charge flowing in the FET channel in a measurement time window of  $\tau$ .  $R$  is a feedback resistor.

Low-noise FETs and TIAs should be used in the circuitry such that the additional noises introduced by these components would not jeopardize the readout of the signal. In addition, high-speed TIAs with a bandwidth of  $>100$  GHz may be required to guarantee a quick readout [45,46]. Although the generation of the voltage signal is an intrinsically fast ( $<100$  fs) process, the response speed of the QCP may be limited by the timing performance of the readout circuitry. Additional delays, such as RC delays caused by metal interconnects, FET gate delays, and transimpedance amplifier group delays, may be added to the overall response time of the QCP. Based on a timing analysis using the delay parameters of state-of-the-art FETs and TIAs, we found a QCP response time of the order of several ps. It is reasonably

optimistic that this response time, which is limited by the speed of the readout circuitry, may march into the sub-ps region with the constant advancing of the semiconductor technology [46]. On the other hand, we remark that the timing jitter of the QCP together with the readout circuit can be in the sub-ps region, thanks to the transport-free quantum capacitive coupling and the superior jitter performance of the recent CMOS technology [47] as well as >100 GHz TIAs (with 0.8 ps timing jitter) [48]. This is to be compared to the timing jitter of ~50 ps achieved recently by superconducting single photon detectors [49].

#### 4. Conclusion

In summary, we proposed a novel quantum capacitive photodetector for registering single photons. The operation of this detector relies on the charge redistribution (that stems from the difference in the shape of GS and ES wave functions) in the QD upon single photon absorption. We implemented the concept in an InAs/AlAs model system by COMSOL simulation, which showed that an output voltage signal of the order of ~4 mV could be created by the detector in response to single photon absorption. Further study suggested that the output signal might be optimized by changing the probe location, or by varying the size or the shape of the QD. To complete the detector design, we suggested a possible readout scheme for the QCP. The photoresponse of the proposed detectors can be engineered in a broad spectral region that ranges from micrometers to millimeters, as the energy spacing between the first excited state and the ground state typically varies from several to hundreds of millielectronvolts. Although we have restricted our discussions to the first excited state case, we remark that similar results can be found if the first excited state wave function used in the simulation is replaced with higher excited state wave functions, for example, second excited state wave function. The non-identical output signals associated with different excited states, in fact, provide the QCP with multi-wavelength detection capabilities. Furthermore, the timing jitter should be minimal in these detectors because there is no carrier drifting or diffusion involved in the detection process, and nearly instantaneous potential change rather than detector current is used as the output signal. For the same reason, the detector response can potentially reach ps regime. With all these merits, quantum capacitive photodetector proposed here marks a paradigm shift in the existing mechanisms for detecting single photons, and may offer new opportunities in emerging quantum information applications.

#### Funding

Defense Advanced Research Projects Agency (DARPA) Army Research Office (ARO) Cooperative Agreement Number (W911NF-16-2-0162).

#### Acknowledgments

This research was sponsored by the DARPA DETECT program through Army Research Office (ARO) Cooperative Agreement Number W911NF-16-2-0162. The views and conclusions contained in this document are those of the authors and should not be interpreted as representing the official policies, either expressed or implied, of the Army Research Office or the U.S. Government. The U.S. Government is authorized to reproduce and distribute reprints for Government purposes notwithstanding any copyright notation herein. J. L. thank Jason Stauth for helpful discussions. J. L. conceived the idea. Y. Z., Y. W., and X. W. conducted the simulation. Y. Z. analyzed the data and wrote the manuscript with the inputs from J. L. and S.-Q. Y. E. R. F. suggested the readout scheme for the QCP. All the authors commented on the manuscript. S.-Q. Y., G. S. and J. L. supervised this work.